



# Dual control of flow field heterogeneity and immobile porosity on non-Fickian transport in Berea sandstone

Filip Gjetvaj, Anna Russian, Philippe Gouze, Marco Dentz

## ► To cite this version:

Filip Gjetvaj, Anna Russian, Philippe Gouze, Marco Dentz. Dual control of flow field heterogeneity and immobile porosity on non-Fickian transport in Berea sandstone. *Water Resources Research*, 2015, 51 (10), pp.8273-8293. 10.1002/2015WR017645 . hal-01278285

**HAL Id: hal-01278285**

**<https://hal.science/hal-01278285>**

Submitted on 11 May 2021

**HAL** is a multi-disciplinary open access archive for the deposit and dissemination of scientific research documents, whether they are published or not. The documents may come from teaching and research institutions in France or abroad, or from public or private research centers.

L'archive ouverte pluridisciplinaire **HAL**, est destinée au dépôt et à la diffusion de documents scientifiques de niveau recherche, publiés ou non, émanant des établissements d'enseignement et de recherche français ou étrangers, des laboratoires publics ou privés.



## RESEARCH ARTICLE

10.1002/2015WR017645

## Key Points:

- We simulate pore-scale flow and anomalous transport in Berea sandstone
- We show that both flow heterogeneity and diffusion in immobile domain control BTC shape
- We upscale successfully the 3-D transport behavior by a new 1-D effective CTRW model

## Correspondence to:

F. Gjetvaj,  
filip.gjetvaj@gm.univ-montp2.fr

## Citation:

Gjetvaj, F., A. Russian, P. Gouze, and M. Dentz (2015), Dual control of flow field heterogeneity and immobile porosity on non-Fickian transport in Berea sandstone, *Water Resour. Res.*, 51, 8273–8293, doi:10.1002/2015WR017645.

Received 3 JUN 2015

Accepted 21 SEP 2015

Accepted article online 23 SEP 2015

Published online 17 OCT 2015

## Dual control of flow field heterogeneity and immobile porosity on non-Fickian transport in Berea sandstone

Filip Gjetvaj<sup>1</sup>, Anna Russian<sup>1</sup>, Philippe Gouze<sup>1</sup>, and Marco Dentz<sup>2</sup>
<sup>1</sup>Géosciences Montpellier, Université de Montpellier, UMR 5243 CNRS, Montpellier, France, <sup>2</sup>Spanish National Research Council (IDAEA-CSIC), Barcelona, Spain

**Abstract** Both flow field heterogeneity and mass transfer between mobile and immobile domains have been studied separately for explaining observed anomalous transport. Here we investigate non-Fickian transport using high-resolution 3-D X-ray microtomographic images of Berea sandstone containing microporous cement with pore size below the setup resolution. Transport is computed for a set of representative elementary volumes and results from advection and diffusion in the resolved macroporosity (mobile domain) and diffusion in the microporous phase (immobile domain) where the effective diffusion coefficient is calculated from the measured local porosity using a phenomenological model that includes a porosity threshold ( $\phi_0$ ) below which diffusion is null and the exponent  $n$  that characterizes tortuosity-porosity power-law relationship. We show that both flow field heterogeneity and microporosity trigger anomalous transport. Breakthrough curve (BTC) tailing is positively correlated to microporosity volume and mobile-immobile interface area. The sensitivity analysis showed that the BTC tailing increases with the value of  $\phi_0$ , due to the increase of the diffusion path tortuosity until the volume of the microporosity becomes negligible. Furthermore, increasing the value of  $n$  leads to an increase in the standard deviation of the distribution of effective diffusion coefficients, which in turn results in an increase of the BTC tailing. Finally, we propose a continuous time random walk upscaled model where the transition time is the sum of independently distributed random variables characterized by specific distributions. It allows modeling a 1-D equivalent macroscopic transport honoring both the control of the flow field heterogeneity and the multirate mass transfer between mobile and immobile domains.

## 1. Introduction

Flow and solute transport in water-saturated porous rock and porous material in general have been the focus of intense research over several decades. The quantification and prediction of observed flow and transport phenomena plays a central role in many areas of science and engineering including groundwater hydrology (e.g., pollution risk analysis and remediation), nuclear waste disposal, underground storage of CO<sub>2</sub> and shale gas exploration [Gouze *et al.*, 2008a; Yoon *et al.*, 2015; Russian *et al.*, 2015], but also transport in biological tissues [Sen and Basser, 2005], for example. The main focus of traditional approaches to quantify effective transport, has been the development of macrodispersion models [Dentz *et al.*, 2011, and literature therein]. The advection-dispersion equation (ADE) is traditionally used to describe transport of nonreactive dissolved chemicals (i.e., tracers) at the Darcy scale. The ADE approach is based on the assumption that the hydrodynamic dispersion, triggered by the combination of the diffusion and the variability of the advective fluxes along the flow paths within the pore space, behaves macroscopically as a diffusion-like (Fickian) process [Bear, 1972]. With  $c(\mathbf{x}, t)$  the concentration of the tracer at position  $\mathbf{x}$  and time  $t$ , the ADE reads:

$$\phi \frac{\partial c(\mathbf{x}, t)}{\partial t} - \nabla \cdot [\mathbf{D} \nabla + \phi \mathbf{u}] c(\mathbf{x}, t) = 0, \quad (1)$$

where  $\mathbf{D}$ ,  $\mathbf{u}$  and  $\phi$  denote the effective dispersion coefficient that quantifies spreading and mixing, the average velocity and the connected porosity respectively. All these parameters are defined at the scale of the support volume, the representative elementary volume (REV), where full mixing of the tracer is assumed [Bear, 1972].

However, many experimental tracer tests, both from in situ [Adams and Gelhar, 1992; Meigs and Beauheim, 2001; Becker and Shapiro, 2003; Gouze *et al.*, 2008b] and laboratory [Kandhai *et al.*, 2002; Levy and Berkowitz,

2003; Scheven *et al.*, 2005; Moroni *et al.*, 2007; Gouze *et al.*, 2009], display strongly asymmetric breakthrough curves (BTCs) with long tails that usually decrease as a power-law of time, whereas the ADE predicts fast concentration decrease. Non-Fickian dispersion manifests itself in power-law tailing of BTCs as well as anomalous scaling of the mean and the variance of the spatial tracer distribution and early arrivals in BTCs [Berkowitz *et al.*, 2006; Neuman and Tartakovsky, 2008]. These numerous experiments indicate that Fickian models fails to capture the real nature of the dispersion in systems macroscopically heterogeneous systems as well as in macroscopically homogeneous such as glass bead columns [e.g., Datta *et al.*, 2013; Holzner *et al.*, 2015].

The apparently ubiquitous non-Fickianity of dispersion in porous media is generally interpreted as the result of the large variability of fluid velocity that is evidently linked to the inherent complexity of the geological formations at all scales. Several authors have explored different approaches (both theoretical and numerical) for characterizing and modeling the processes that control non-Fickian dispersion in relation with the geometry of the pore space [e.g., Bijeljic and Blunt, 2006; Le Borgne *et al.*, 2011; de Anna *et al.*, 2013; Holzner *et al.*, 2015] and at larger scale to the heterogeneous distribution of the hydraulic conductivity field [e.g., Ederly *et al.*, 2014].

In the present paper we focus on macroscopic non-Fickian behavior arising from (stationary) pore-scale Navier-Stokes flow of a Newtonian fluid in a relatively simple natural porous rock. It has been possible only recently to systematically investigate these type of problems due to the possibility of accurately imaging natural porous structures by X-ray micro-tomography (XRMT) tools [Ovaysi and Piri, 2011; Blunt *et al.*, 2013]. The common approach is to process XRMT images in order to distinguish the pore from the solid, then simulate the steady-state flow of an incompressible fluid and finally solve the diffusion-advection equation in order to obtain the distribution of the tracer concentration according to specified boundary conditions [Blunt *et al.*, 2013]. Then, the tracer spreading is analyzed in relation with the flow field properties for different values of the average velocity that determines the contribution of the diffusion in the tracer transport [Bijeljic *et al.*, 2013a]. The pertinence of the analysis depends strongly on the accuracy of the calculations and the representativeness of the domain size, which in turn are strongly dependent both on the technological XRMT and computational limitations [Arns *et al.*, 2005; Guibert *et al.*, 2015a] and on the relevance of the image data processing [Schlüter *et al.*, 2014]. Nevertheless this approach is unmatched for investigating spreading and mixing processes arising from the wide range of transit times experienced by the tracer when transported across the pores of different size and shape.

Few recent studies have focused on the investigation of the relations between the (wide) velocity variability and consequently the (wide) range of transit times of a transported inert tracer using direct pore flow simulations in simple structures [e.g., Le Borgne *et al.*, 2011; de Anna *et al.*, 2013], glass bead packs [e.g., Maier *et al.*, 2008; Holzner *et al.*, 2015], sandstones [e.g., Kang *et al.*, 2014] and carbonate rock [e.g., Bijeljic *et al.*, 2013a, 2013b]. For instance, Bijeljic *et al.* [2011] studied the transport of a passive tracer in small volumes of Berea sandstone (the same rock type as the one used in the present paper) and a Portland limestone following the methodology presented above (i.e., based on the direct calculation of the Stokes flow on digitized XRMT images). The authors (op. cit.) computed the average travel time distribution as the function of the Peclet number using a streamline-based random walk approach. Finally, these transition time distributions were modeled as truncated power-laws [Dentz *et al.*, 2004] and then used to parametrize a continuous time random walks (CTRW) model. Kang *et al.* [2014] studied the purely advective transport of a tracer in a small volume of Berea sandstone as well. However, these authors (op. cit.) interpreted the anomalous dispersion as the results of correlation features of the Lagrangian velocities that can be accounted for in a CTRW model. CTRW characterized by a correlated random time increment was initially proposed by Le Borgne *et al.* [2011] and [de Anna *et al.*, 2013] to model transport in simple 2-D structures where the anomalous dispersion arises from the competition between distribution and correlation effects of the velocity.

Matrix diffusion represents another critical transport process that controls the late-time behavior of BTCs [e.g., Haggerty and Gorelick, 1995; Carrera *et al.*, 1998; Shapiro, 2001; Zhou *et al.*, 2007; Gouze *et al.*, 2008a]. The tracer transit times by diffusion in the matrix are usually orders of magnitude larger than the average transit time in the connected porosity controlling the medium permeability. If a fraction of the medium is formed of the matrix where diffusion is dominant, then dual-porosity models can be conveniently used. Mass transfer between mobile and immobile zones and the separation of characteristic transport time scales in the mobile and immobile regions gives rise to non-Fickian transport behaviors. These mechanisms

are quantified by the multirate mass transfer ADE model (MRMT-ADE) [Haggerty and Gorelick, 1995; Carrera et al., 1998; Haggerty et al., 2000], which can be formulated as

$$\xi_v \frac{\partial c(\mathbf{x}, t)}{\partial t} - \nabla \cdot [\mathbf{D} \nabla + \xi_v \mathbf{u}] c(\mathbf{x}, t) + S(\mathbf{x}, t) = 0 \quad (2)$$

with the sink-source term

$$S(\mathbf{x}, t) = \xi_\mu \frac{\partial}{\partial t} \int dt' M(t-t') c(\mathbf{x}, t'), \quad (3)$$

where  $\xi_v$  and  $\xi_\mu$  denote the volume fraction of the mobile domain (i.e., the macroscopic connected porosity) and the volume fraction of the immobile domain respectively; and  $M(t)$  is the memory function that contains all the information on the mass transfer process, the geometry and the volume fraction of the immobile domain as well as its accessibility to tracer particles issued from the mobile domain. A power-law designed memory function will trigger the power-law tail of the BTCs. Specifically, a power law tailed BTC that decays as  $\propto t^{-\beta-1}$  corresponds to  $M(t) \propto t^{-\beta}$ . This behavior would persist infinitely if the tracer could assess longer diffusion paths as time increases, such as in fractal systems. However, a maximum diffusion length is expected in natural porous media displaying finite size immobile domains and  $M(t)$  decays exponentially fast to zero when the maximum residence time in the immobile domain is reached and the system evolves toward asymptotic Fickian dispersion according to (2). The MRMT-ADE approach accounts also for the heterogeneity of the matrix, and has been successfully applied to model field and laboratory experiments [Haggerty et al., 2001, 2004; Gouze et al., 2008a]. The MRMT-ADE and the CTRW approaches are equivalent under certain conditions as discussed in Dentz and Berkowitz [2003] and Schumer et al. [2003].

In the studies cited above the origin of the non-Fickian dispersion has been investigated either considering the void and the solid phases to tackle the effects of the velocity distribution in the mobile domain, or considering the effect of an immobile domain while the dispersion was assumed Fickian in the mobile domain. Here we will investigate both mechanisms by considering simultaneously the presence of the matrix where transport is controlled by diffusion and the velocity variability in the mobile domain. The presence of microporous material in reservoir rocks, for instance detected by XRMT imaging, and its control on the connectivity and consequently its permeability has been documented in recent studies [Gouze et al., 2008a; Mangane et al., 2013; Garing et al., 2014; Hebert et al., 2015].

The paper is organized as follow. Section 2 describes image acquisition and segmentation. In section 3, we present the methods used to perform flow simulations, and the particle tracking methods. Section 4 is dedicated to the analysis of the results of the particle transport simulations and their discussion. Conclusions are presented in section 5.

## 2. Rock Sample Imaging

Berea sandstone has been used extensively as a sandstone reservoir proxy because it is relatively homogeneous, cohesive, well characterized and easily available [Churcher et al., 1991; Øren and Bakke, 2003; Tanino and Blunt, 2012]. Berea sandstone is composed of quartz grains that are cemented together by silica, dolomite, feldspar, and clayey minerals. Grains are well sorted (ranging in size between 70 and 400  $\mu\text{m}$ ) and well rounded (only around 20% of grains are not spherical) [Churcher et al., 1991]. Cement fraction in Berea sandstone ranges from 1.8 to 9% [Øren and Bakke, 2003; Tanino and Blunt, 2012]. Here we intentionally chose a sample with the lowest cement fraction in order to determine if a low fraction of immobile domain can produce a key control on the dispersion together with the velocity heterogeneity in the mobile domain.

### 2.1. Image Acquisition

The high resolution X-ray microtomography (XRMT) image of the core (10 mm length and 6 mm diameter) was acquired using the BM5 beamline at the European Synchrotron Radiation Facility (Grenoble, France). The 3-D volume was reconstructed from 3495 projections acquired at an energy of 110 keV using a GGG:Eu 100 microns scintillator and a SCMOs-based  $2048 \times 2048$  pixels detectors (model PCO edge; <http://www.pco.de>). The reconstruction was performed using the single distance phase retrieval algorithm described by Paganin et al. [2002] applying an unsharp filter before reconstruction. Details on the reconstruction algorithm and performances can be found in Sanchez et al. [2012]. The final 3-D image is formed by  $4667 \times$

2130 × 2099 voxels of characteristic size 3.16 μm (3.16 × 10<sup>−6</sup> m). The 16 bits encoded value associated to each of the voxels denotes the X-ray absorption integrated over a volume of 31.5 μm<sup>3</sup>.

## 2.2. Identification of the Different Type of Porosity

Analysis of the raw XRMT images pointed out the existence of three types of material, denoted hereafter phases. The three phases correspond respectively to the macroporosity (i.e., the void space filled with water or air), the microporosity (voxels in which pores are smaller than image resolution) and the solid rock. The identification and then labeling of these three phases is called segmentation. There are different methods for performing image segmentation, none of them producing strictly equivalent results. Segmentation is consequently a critical step of the data processing [Iassonov et al., 2009; Schlüter et al., 2014; Scheibe et al., 2015].

Global thresholding is often applied; this simple approach consists in deciding a gray scale value separating two material types on the basis of image histogram analysis. However, by definition the microporous material can display a large range of gray level values depending on its porosity, while intermediate gray level values denote pixels sampling both solid and voids. Consequently, it is a priori not pertinent to use the global thresholding method for the present study where the presence of heterogeneous microporous material is known. Several alternative methods have been developed in order to improve the accuracy of the segmentation; see the comparative study by Iassonov et al. [2009].

Here we use the so called “region growing” methods based on the assumption that all the voxels belonging to a given phase cluster are connected and are similar in terms of gray levels [Spirkovska, 1993]. A significant difficulty of region growing methods is the need for carefully defining the initial gray level range, limiting the seed regions for each phase, which is typically done manually from analyzing the histogram. However, the image histogram does not contain enough information to properly identify the different phases, and relatively small differences on the threshold values may induce noticeable errors on the determination of the phase fractions. Here we applied the method proposed by Mangane et al. [2013] that consists in conditioning the determination of the threshold values (delimiting the initial gray level range for each phase) by the value of the total porosity measured independently using laboratory techniques. For delimiting the three phases four thresholds values must be determined. The convergence toward a satisfactory agreement between the measured total porosity and that obtained by the segmentation procedure ( $\phi_t$ ) is obtained from an iterative procedure, where  $\phi_t$  is:

$$\phi_t = \xi_v + (\xi_\mu \phi_\mu) \quad (4)$$

with  $\xi_v$  and  $\xi_\mu$  the volume fraction of the void phase (macroporosity) and of the microporous material, respectively, and  $\phi_\mu$  the intrinsic porosity of the microporous phase. Here we used the porosity evaluated from mercury intrusion porosimetry (MIP) as the reference total connected porosity. This procedure was applied to the gray level image assuming that first the mineralogical composition of the microporous cement is homogeneous, and second that the porosity of the microporous phase range from 0.01 to 60%. This later assumption is based on the fact that above 60% the material cannot be cohesive. The procedure is based on comparing the experimental porosity to the total porosity (4) where  $\xi_v$  may contains pixels belonging to porosity unconnected to the percolating cluster. However, we measured the value of this unconnected porosity a posteriori (see in section 2.3) and found that it was always lower than 0.8% for each of the studied subvolumes. Accordingly one can consider that this value represents the error on the segmentation. The average porosity of the microporous phase is 24.93%, and the total porosity calculated by equation (4) is 18.8%. Figure 1 illustrates the pore network and microporosity obtained by three phase segmentation.

## 2.3. Microporosity and Connected Clusters

Figure 2 illustrates the throat radius distribution obtained by MIP test. The throat radius distribution for the Berea sandstone under consideration is quite narrow compared to other rocks, especially carbonates. Most throat radii are between 8 and 20 μm, but there is a significant portion of throats with smaller radii. The dashed line in Figure 2 marks the XRMT image voxel size. All throats and pores with smaller radii cannot be distinguished on the XRMT images and are assigned to the microporous phase.

In the following, flow and transport will be studied on 4 nonoverlapping subvolumes (SV1, SV2, SV3, and SV4) of 300 × 300 × 300 voxels randomly extracted from the full core image. In order to investigate the



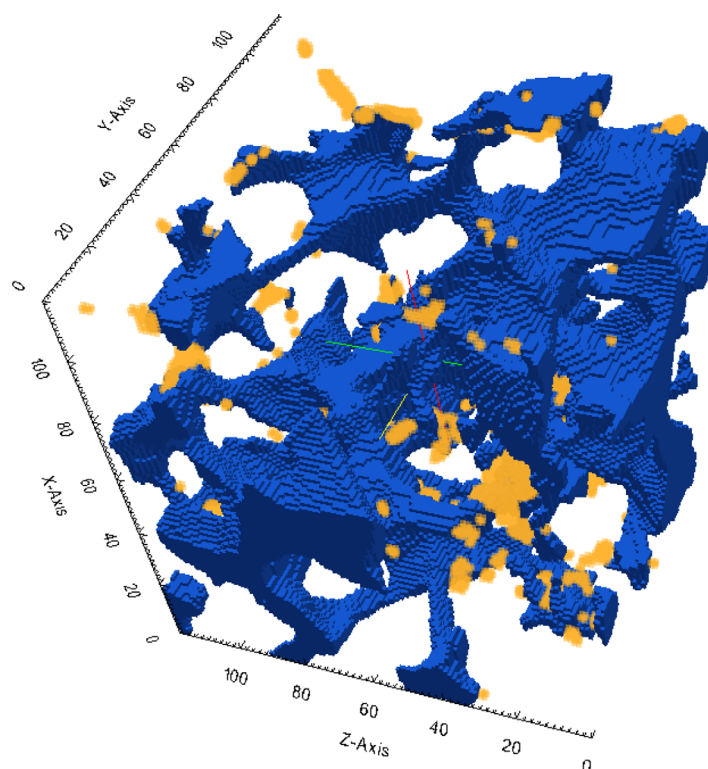


**Figure 1.** Three-dimensional visualization of the pore network (blue) and the connected microporosity (yellow) for a subvolume of  $120 \times 120 \times 120$  voxels.

perpendicular to the flow direction in subvolume SV1 for the two-phase segmented image (Figure 3a) and for the three-phase segmented image (Figure 3b). One can see, for example in the area marked by the green circle, that the three-phase image contains a fraction of macroporosity connected that is connected by microporous material (in orange), a feature that does not exist in the two-phase image. The porosities for the four subvolumes are given in Table 1. The total porosity  $\phi_t$  of the three-phase subvolumes calculated by (4) is on average increased by 5.3% when compared to the equivalent two-phase volume.

This corresponds to an average increase of a 2% of the macroporosity, which is made accessible by the microporous cement clusters. By definition, this fraction of the macroporosity belongs to the immobile domain because transport is only due to diffusion.

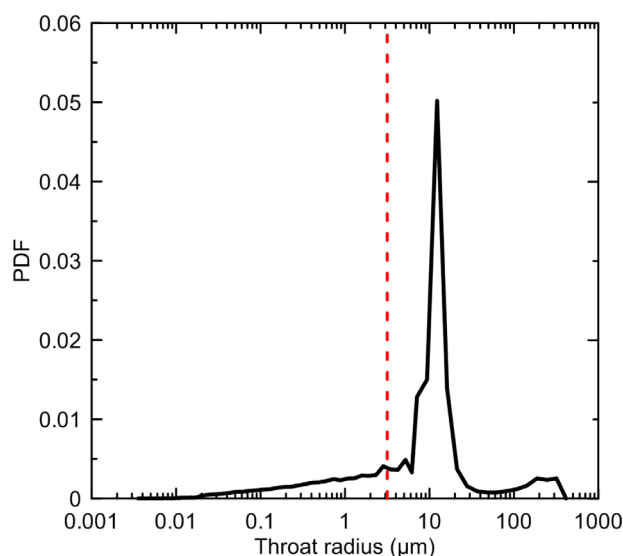


**Figure 2.** Throat radius PDF obtained from mercury intrusion porosimetry for Berea sandstone. The vertical dashed line marks the XMRT image voxel size.

influence of microporosity on solute transport we compare flow and transport computed on the three-phase segmented volumes, and two-phase images where the microporous phase is assigned to the solid phase.

The first step of the segmented-data processing consists in the determination of the percolating clusters, i.e., the computation of the network of pores that spans through the whole volume and connects the boundaries in flow direction. Percolated clusters were identified using the method described in *Hoshen and Kopelman* [1976]. The mobile domain, in which the flow will be computed corresponds to the connected macroporosity, while the immobile domain corresponds to the microporosity as well as a fraction of the macroporosity that is connected by the microporous phase only. Figure 3 shows the same cross sections

### 3. Modelling Tools

#### 3.1. Mesh Generator

*Guibert et al.* [2015a] showed that the grid resolution is an important issue for ensuring meaningful permeability calculations. Here we want to investigate the influence of the grid resolution on the calculation of the transport properties as well. Therefore, we first programmed a new meshing algorithm that is capable to create regular hexahedron mesh compatible with OpenFOAM® strictly equivalent to the voxels of the segmented images. Applying this

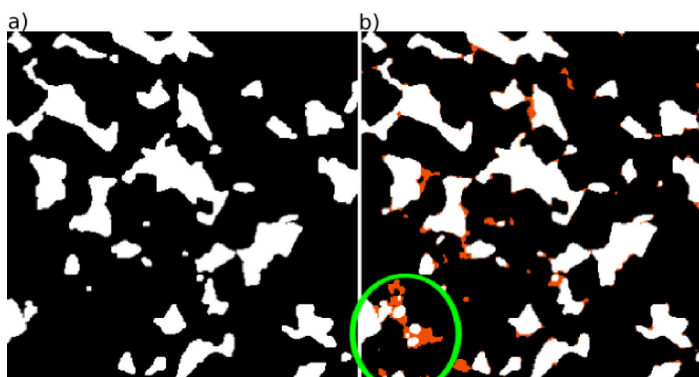


**Figure 3.** Comparison between a cross section ( $300 \times 300$  pixels) extracted from subvolume SV1 perpendicular to the flow direction for (a) a two-phase image and (b) a three-phase image. Black areas denote the solid phase (no advection and no diffusion), white areas denote the macroporosity, i.e., the mobile domain and areas colored in orange indicate the microporous phase where transport is assumed to be controlled by diffusion only.

algorithm we are able to avoid any averaging or smoothing that often occur in the course of the standard OpenFOAM<sup>®</sup> meshing procedure. Then we built two meshes with different resolution for each of the subvolumes (SV1–SV4). The hereafter called “coarse mesh” is made of cubic cells with the same size as the image voxels, while the “fine mesh” is obtained by dividing each voxel by 3 in all the directions, creating consequently 27 cubes of  $1.05 \mu\text{m}$  size per image voxel.

### 3.2. Solving Flow

Single phase flow in porous media on pore-scale is classically calculated by the Navier-Stokes equation [Bear, 1972; de Marsily, 1986]. In this work, we computed the pore-scale flow field by solving the conservation equation (5) and the Navier-Stokes equation (6), for single-phase with a constant density and viscosity.

$$\nabla \cdot u = 0 \quad (5)$$

$$\rho \left( \frac{\partial u}{\partial t} + u \cdot \nabla u \right) = -\nabla p + \mu \nabla^2 u, \quad (6)$$

where  $u$  denotes the velocity vector (m/s),  $\rho$  is the fluid density ( $\text{kg/m}^3$ ),  $t$  is the time,  $p$  is pressure (Pa) and  $\mu$  is fluid viscosity (Pa s).

Equations are solved by using the steady-state solver based on the SIMPLE algorithm implemented in OpenFOAM<sup>®</sup> [Weller et al., 1998]. OpenFOAM is a free, open source computational fluid dynamics software package with parallelization capabilities. The equations are discretized using the finite volume method. The SIMPLE (Semi-Implicit Method for Pressure-Linked Equations) algorithm presented by Patankar [1980], is one of the pressure-based method techniques to solve pressure-velocity coupling. It allows to iteratively solve Navier-Stokes equation and obtain the steady state pressure and velocity fields. For each step pressure and velocity field are calculated according the boundary conditions and the results from the previous step, until the difference between the current and previous steps is smaller than a given convergence criterion.

**Table 1.** Total Porosity ( $\phi_t$ ; see (4)) for Two-Phase and Three-Phase Images, Columns 1 and 2, Respectively<sup>a</sup>

	Total Porosity $\phi_t$		Relative Difference (%)	
	Two-Phase	Three-Phase	$\Delta\phi_t$	$\Delta\phi_v^{\varepsilon}$
SV1	19.36	20.37	5.25	1.97
SV2	19.32	20.23	4.68	1.56
SV3	18.26	19.18	5.03	2.04
SV4	18.21	19.33	6.14	2.51

<sup>a</sup>Column 3: relative difference between total porosity  $\Delta\phi_t = [\phi_t^{(3P)} - \phi_t^{(2P)}] / \phi_t^{(3P)}$ . Column 4 reports the relative difference between the fraction of the void phase included in the total porosity:  $\Delta\phi_v^{\varepsilon} = [\varepsilon_v^{(3P)} - \varepsilon_v^{(2P)}] / \varepsilon_v^{(3P)}$ . This difference denotes the fraction of macroporosity made accessible to diffusion due to the presence of the microporous phase.

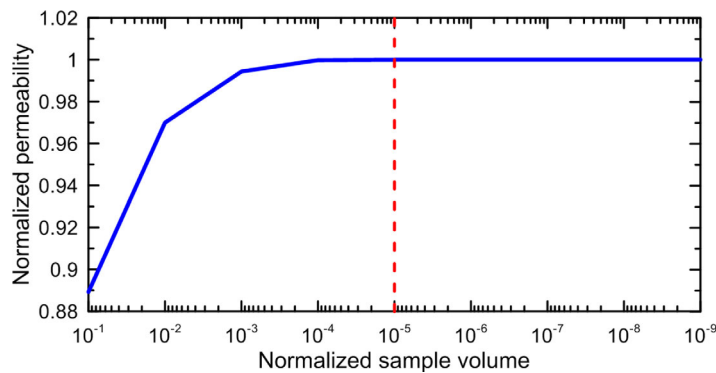


**Figure 4.** Normalized permeability as a function of the sample volume for different residual convergence criteria.

Constant pressure is applied to the inlet and outlet boundaries while all other boundaries including the void-rock interface are considered as no-flow boundaries (no-slip condition at the void-rock interface). Twenty layers of void voxels have been added to the porous volume at the inlet and outlet boundaries in order to minimize the boundary effect [Guibert *et al.*, 2015b]. Fluxes at the inlet and outlet boundaries and residual convergence were used to evaluate if the simulations have fully converged. To determine the residual convergence criterion, we made several simulations on the same structure while constantly decreasing the convergence criterion until the computed permeability converged to a stationary value. For the Navier-Stokes flow simulations described below, the computation duration, using a 24-cores Intel Xeon (2.3 GHz) PC, ranged from about 10 h for a  $300^3$  voxels mesh to about 75 h for a  $900^3$  voxels mesh.

Permeability  $k$  was calculated from Darcy's law

$$k = \frac{\mu Q L_z}{\Delta p A_z} \quad (7)$$

where  $Q$  is the total flux ( $\text{m}^3/\text{s}$ ),  $L_z$  length of the block in flow direction, and  $A_z$  ( $\text{m}^2$ ) is the area of the cross section perpendicular to the flow direction.

Figure 4 displays the permeability values obtained for different values of the residual convergence criterion. We observed that the computed permeability value increases with the decrease of the fixed convergence residual and eventually stabilizes after the initial residual falls below  $10^{-4}$ . Based on these results we decided to use  $10^{-5}$  as the residual convergence criteria which has proved to give completely converged calculations with reasonable computation times.

All simulations were made with low Reynolds numbers of  $Re \cong 10^{-6}$ . The Reynolds number is defined as the ratio of viscous and inertial forces,  $Re = (\rho \bar{u} L) / \mu$ , where  $\bar{u}$  is the average superficial velocity [ $\text{m/s}$ ] and  $L$  is characteristic length [ $\text{m}$ ]. For such low values of  $Re$  flow is laminar, and formation of eddy-currents, which could create anomalous dispersion, is minimized.

Figure 5a presents the probability density function (PDF) of velocity in flow direction. We observe that velocity values are mainly positive. Yet the small portion of negative values emphasizes the complexity of the pore network. The PDF of velocities perpendicular to the flow direction are displayed in Figure 5b, where we observe similar distributions of negative and positive velocities, as expected for an macroscopically homogeneous, isotropic volume of rock.

### 3.3. Solving Transport

Pore-scale transport in the mobile domain is computed by solving the advection-diffusion equation

$$\frac{\partial c(\mathbf{x}, t)}{\partial t} - \nabla \cdot [d_0 \nabla + \mathbf{u}(\mathbf{x})] c(\mathbf{x}, t) = 0, \quad (8)$$

where  $d_0$  is the diffusion coefficient of the tracer in water and  $\mathbf{u}(\mathbf{x})$  is the flow velocity. Here we solve (8) using the time domain random walk (TDRW) method [Noetinger and Estebenet, 2000; Delay and Bodin, 2001; Delay *et al.*, 2005]. Details about the implementation of the TDRW approach, starting from the discretization of the transport equation up to the random walk algorithm implementation can be found in Dentz *et al.*



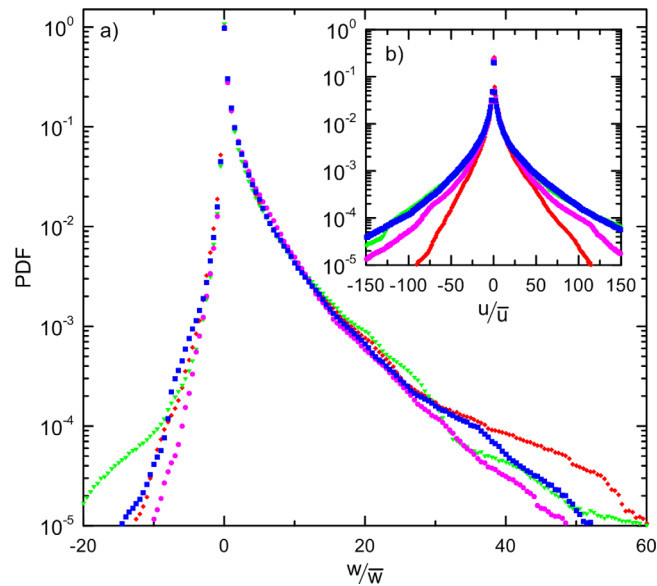


**Figure 5.** PDFs of normalized velocity for the four subvolumes (a) along the main flow direction ( $w$ ) and (b) perpendicular to the main flow direction ( $u$ ) for subvolume 1 (red rhombi), subvolume 2 (green triangles), subvolume 3 (magenta circles), subvolume 4 (blue squares).

[2012]. The domain discretization is the same as the one used for computing the flow field and corresponds to the image voxels (coarse mesh) or the image voxel divided in 27 cubes (fine mesh) as explained in section 3.1. The TDRW approach models particle motions in space and time by the following recursive relations

$$\mathbf{x}_i(n+1) = \mathbf{x}_j(n) + \xi_{ij}, \quad t(n+1) = t(n) + \tau_j. \quad (9)$$

The probability  $w_{ij}$  for a transition of length  $|\xi_{ij}|$  from pixel  $j$  to pixel  $i$ , and the transition time  $\tau_j$  associated to pixel  $j$  are given by

$$w_{ij} = \frac{b_{ij}}{\sum_{|jk|} b_{kj}}, \quad \tau_j = \frac{1}{\sum_{|jk|} b_{kj}}, \quad (10)$$

where the notation  $\sum_{|jk|}$  denotes summation over the nearest neighbors of pixel  $j$ . The  $b_{ij}$  are defined as follows,

$$b_{ij} = \frac{\hat{d}_{ij}}{\xi_{ij}^2} + \frac{|u_{ij}|}{2\xi_{ij}} \left( \frac{u_{ij}}{|u_{ij}|} + 1 \right), \quad (11)$$

where  $\xi_{ij} = |\xi_{ij}|$ ;  $\hat{d}_{ij}$  is the harmonic mean of the diffusion coefficients of pixels  $i$  and  $j$ ;  $u_{ij}$  denotes the velocity component of  $\mathbf{u}_j$  in the direction of pixel  $i$ ,  $u_{ij} = \mathbf{u}_j \cdot \xi_{ij}$ . If  $u_{ij} > 0$ , pixel  $i$  is downstream from pixel  $j$ , and correspondingly, if  $u_{ij} < 0$  pixel  $i$  is upstream from pixel  $j$ .

The TDRW method is used to solve transport in both the mobile and the immobile domains, where for the latter the velocity is zero. Accordingly the transport equation in the immobile domain (i.e., in the microporous phase) is:

$$\phi_\mu(\mathbf{x}) \frac{\partial c(\mathbf{x}, t)}{\partial t} - \nabla \cdot [d^e(\mathbf{x}) \nabla c(\mathbf{x}, t)] = 0, \quad (12)$$

where  $d^e$  is the spatially distributed effective diffusion coefficient in the immobile domain:

$$d^e(\mathbf{x}) = \tau_\mu^{-1}(\mathbf{x}) \phi_\mu(\mathbf{x}) d_0, \quad (13)$$

where  $\tau$  denotes the tortuosity of the immobile domain, which is usually expressed as a power-law of the porosity,  $\tau_\mu \equiv \phi_\mu^{-m}$  [Pisani, 2011]. Furthermore, for porosity values smaller than the porosity  $\phi_\theta$  at the percolation threshold, no more diffusion can take place. Thus, the effective diffusion coefficient  $d^e$  takes the following form,

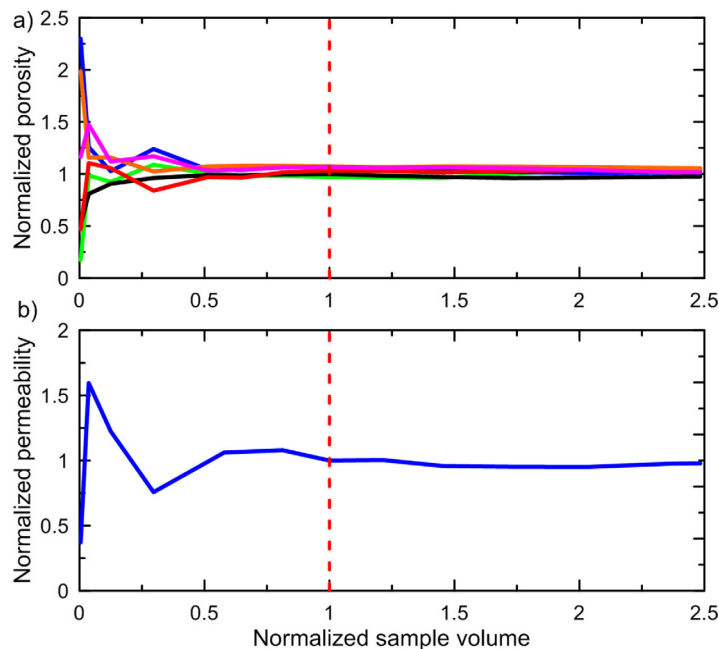


**Figure 6.** (a) Normalized porosity and (b) permeability versus the sample volume normalized by the reference volume of  $300^3$  voxels.

$$d^e(\mathbf{x}) = \begin{cases} \phi_\mu(\mathbf{x})^n d_0 & \text{for } \phi_\mu > \phi_\theta \\ 0 & \text{for } \phi_\mu < \phi_\theta \end{cases} \quad (14)$$

with  $n = m + 1$ . In the following we will test different values of  $n$  from  $n = 1$  up to  $n = 4$  [Gouze *et al.*, 2008a], because we have no information on the exact value of  $n$ . Note that  $\phi_\theta$  is a characteristic property of the porous material under consideration and requires an experimental approach to be determined precisely. In our case the value of  $\phi_\theta$  is not known. In the following, we test the sensitivity of the results to this parameter for different values ranging from  $\phi_\theta = 0$  up to  $\phi_\theta = 0.4$ .

### 3.4. Representativeness of the Samples

For simulating flow and transport in heterogeneous porous media it is essential that the support volume used for the calculations is large enough to be representative of the medium. The minimum volume required is the representative elementary volume (REV) [Bear, 1972]. To evaluate the representativeness of the  $300^3$  voxel subvolumes SV1–SV4, we made calculations of the porosity and the permeability of the mobile domain for increasing size of the support volume. For porosity we randomly chose 6 locations in the core and measured the mobile domain porosity for cubes of increasing size. For permeability we followed the same procedure, but starting from one location only, in order to keep this study tractable in terms of computational times. For the same reason we performed the Navier-Stokes computations using the coarse mesh (i.e., mesh cells of the same size as the image voxels) in order to be able to increase the support volume sufficiently for a sound evaluation of the size effect.

Figure 6a presents results of the mobile domain porosity as a function of the support volume. The plotted porosity values are normalized to the porosity of the whole image and the volume values are normalized to the volume of the  $300^3$  voxel subvolumes (i.e.,  $0.95 \text{ mm}^3$ ). Although there are small differences in the asymptotic porosities (which denotes large scale variability of the porosity in the core) depending on the initial location, we concluded that porosity stabilizes for volumes of about 0.5 times that of the  $300^3$  voxel sample. Similar behavior was observed for the permeability calculations; the relative difference in permeability is staying below 5% for all subvolumes larger than  $300^3$ . Together with the observations made on the velocity PDF (section 3.2), one can conclude that  $300^3$  voxels subvolumes can be considered as a good approximation of a REV in terms of porosity and flow in the mobile domain, albeit they may display weak differences in their macroscopic properties.

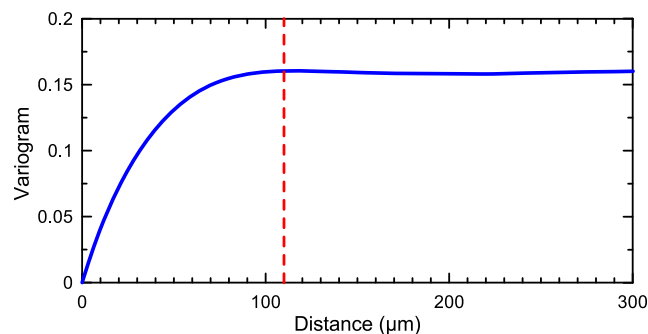


Figure 7. Porosity variogram for the Berea sandstone sample.

### 3.5. Transport Characterization

At the pore-scale, tracer transport is driven by both advection and diffusion. The relative importance of these two mechanisms is quantified by the Peclet number  $Pe$  [de Marsily, 1986]:

$$Pe = \frac{\bar{u}L}{d_0} \quad (15)$$

where  $d_0$  is the coefficient of molecular diffusion (set here to  $10^{-9} \text{ m}^2 \text{ s}^{-1}$ ) and  $\bar{u}$  the average pore velocity. The characteristic length  $L$  is usually associated with the average pore diameter in relation with the definition of  $Pe$  in a capillary [Taylor, 1953]. For the heterogeneous pore structure under consideration here, we define the characteristic length  $L$  from variogram of the porosity of the mobile domain, which is displayed in Figure 7. The dashed line indicates the length ( $\approx 110 \text{ } \mu\text{m}$ ) at which the variogram reaches its asymptotic value. This is considered here as the characteristic length  $L$ . In order to make our results comparable to those of Mostaghimi *et al.* [2012], we applied also the simplified method they proposed, which is based on the assumption that the sandstone is made of regularly packed spheres. For this idealized system, the characteristic length can be associated with the sphere diameter  $L = \pi V \sigma^{-1}$ , where  $V$  is total volume and  $\sigma$  is the interface area between the mobile domain and the solid phase. Applying this method to our subvolumes one obtains values ranging from 122.1 to 125.6  $\mu\text{m}$ , which are similar to those obtained from the variogram method. We note that this evaluation of  $L$  is in good argument with the characteristic lengths calculated for Berea sandstone in other studies ( $L = 131.13 \text{ } \mu\text{m}$  [Mostaghimi *et al.*, 2012],  $L = 100 \text{ } \mu\text{m}$  [Bijeljic *et al.*, 2004]) and  $L = 150 \text{ } \mu\text{m}$  [Øren and Bakke, 2003]).

## 4. Results and Discussion

Here we present and discuss the results obtained from the calculation of tracer transport in subvolumes SV1–SV4. Figures 8–16 show the breakthrough curves (BTC) at the outlet of the subvolumes. The BTC measures the number  $Np$  of particle observed at the outlet normalized by the total number  $Np_0$  of particle injected at the inlet. The simulations use  $Np_0 = 10^6$  particles. The computation time for the transport simulations discussed below ranged from about 10 min to 30 h using a 12-cores Intel Xeon (2.6 GHz) computer, and depends mainly on the value of the Peclet number and the presence and properties of the immobile domain.

We first study the influence of the mesh resolution on the resulting BTCs and then analyze the respective controls of advection and diffusion in the mobile domain, and mass transfer between the mobile and the immobile domains. The results depend on the Peclet number that characterizes the relative strength of diffusion and advection in the mobile domain, and the parameters which characterize the effective diffusion in the immobile domain, i.e., the exponent  $n$  and the percolation threshold  $\phi_\theta$  in (14).

### 4.1. Influence of the Mesh Resolution

For all the simulations presented here, we fixed the value of  $Pe$  by multiplying the flow velocity by a coefficient in order to obtain the required average velocity. Nevertheless, when comparing meshes with different resolutions one must take into account that the permeability computed by equation (7), and consequently the average velocity, are slightly different depending on the voxel size. For subvolume SV3 the permeability

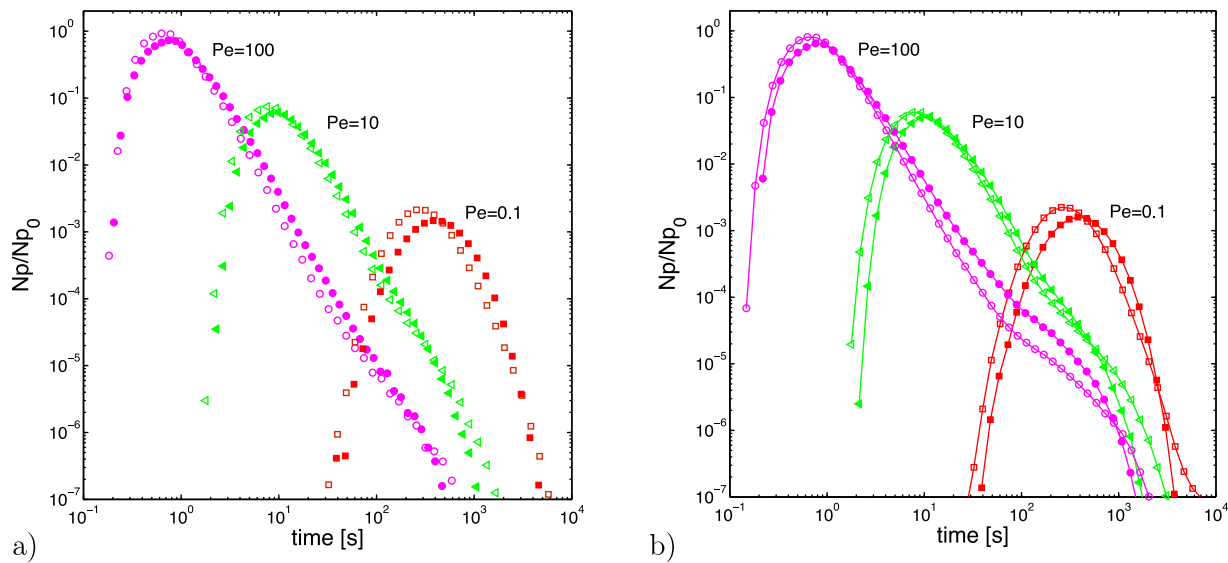
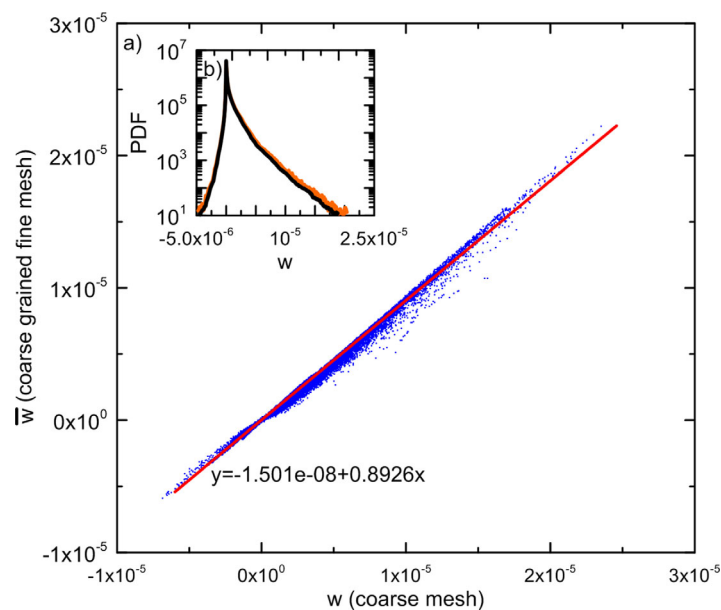


**Figure 8.** BTC obtained with the coarse mesh (300<sup>3</sup> cells, open symbols) and fine mesh (900<sup>3</sup> cells, full symbols) for subvolume 3 for  $Pe = 100$  (pink circles),  $Pe = 10$  (green triangles), and  $Pe = 0.1$  (red squares). (a) The BTCs for mobile transport only, and (b) mobile transport and diffusion in the microporous phase.

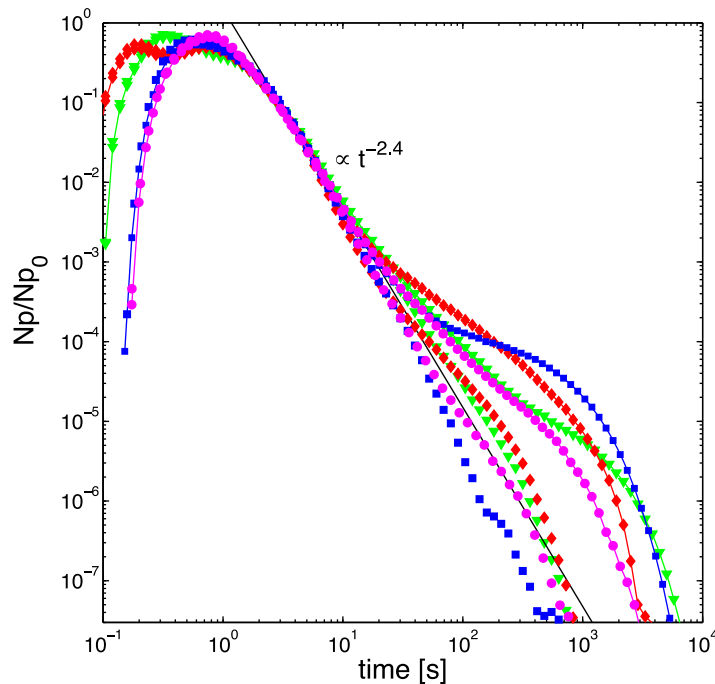
is 867 mD for coarse mesh and 753 mD for fine mesh. This decrease of permeability with the voxel size was already mentioned by Guibert *et al.* [2015a]. To make the comparison meaningful, we first calculate the multiplication factor for the targeted Peclet number for the fine mesh and used the same coefficient to multiply the flow velocity for the coarse mesh.

Figure 8 displays the BTCs for the coarse and fine meshes for different transport regime ( $Pe=0.1$ , 10 and 100). Figure 8a shows BTCs for transport in the mobile domain only, while Figure 8b shows BTCs for transport in the presence of mass transfer between the mobile and immobile domains.

For both cases (i.e., with and without immobile domain) we observe that for advection dominated transport ( $Pe=100$ ) the peak arrival time for the fine mesh is around 20% larger than for the coarse mesh. This is a



**Figure 9.** (a) Cross plot of coarse grained velocities for subvolume 3 versus the velocity average over the coarse cell obtained from the fine mesh data (blue points) together with the best-fit (red line). (b) Inset: PDFs of velocity along the main flow direction  $w$  for the (black) fine mesh and (orange) coarse mesh.



**Figure 10.** BTC for subvolumes SV1 (red rhombi), SV2 (green triangles), SV3 (pink curves), and SV4 (blue squares) for  $Pe = 100$ . Unconnected symbols denote simulations with transport in the mobile domain only and line-connected symbols denote simulations with diffusion in the immobile domain, setting  $n=1$  and  $\phi_0=0$  in equation (14).

direct consequence of the higher average velocity and permeability in the coarse mesh. There are also slight differences in the concentration decay after the peak, which are more marked for the mobile-immobile case. For diffusion dominated transport characterized by  $Pe=0.1$ , the peak arrival time for the fine mesh is around 50% longer than for the coarse mesh. This 50% difference in the peak concentration arrival time is larger than the difference in the permeability. The BTC for the coarse mesh and  $Pe=0.1$  (Figure 8b)

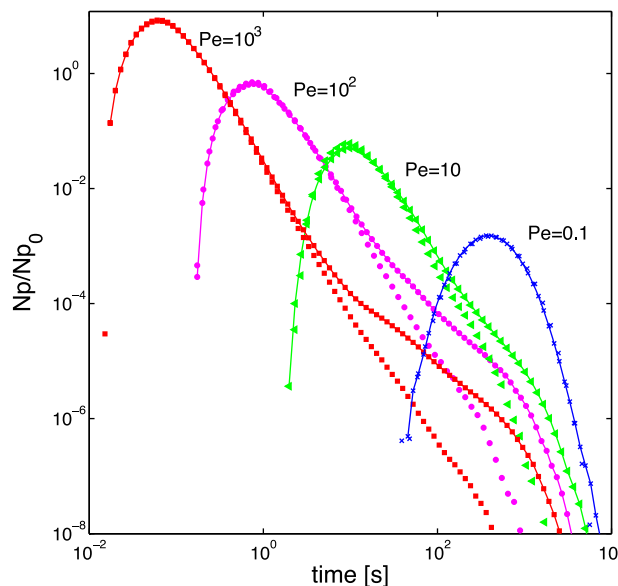


**Figure 11.** BTC for subvolume 3 (SV3) computed with transport in the mobile domain only (unconnected symbols), and with the immobile domain (connected symbols) for  $Pe = 1000$  (squares),  $Pe = 100$  (circles),  $Pe = 10$  (triangles), and  $Pe = 0.1$  (crosses) with  $n = 1$  and  $\phi_0 = 0$  in equation (14).

also displays an extended tailing. Regarding the maximum concentration values one observes that they are always higher for the coarse mesh than for the fine mesh, with differences ranging between 18% and 29% in the simulations without immobile domain and 15–20% for the case with mobile-immobile mass transfer. These results indicate that an insufficient mesh resolution can lead to an overestimation of the anomalous transport characteristics by increasing peak concentrations, decreasing peak arrival times, and increasing tailing; these effects are more pronounced at low Peclet numbers. However, the origin of these differences is not clear. Figure 9 presents a detailed investigation of the differences in the flow field for different mesh resolutions. For the fine mesh we performed a coarse graining process in which the mean velocity is calculated from the 27 mesh cells (dividing by each voxel by 3 in for each direction) which belong to each of the void



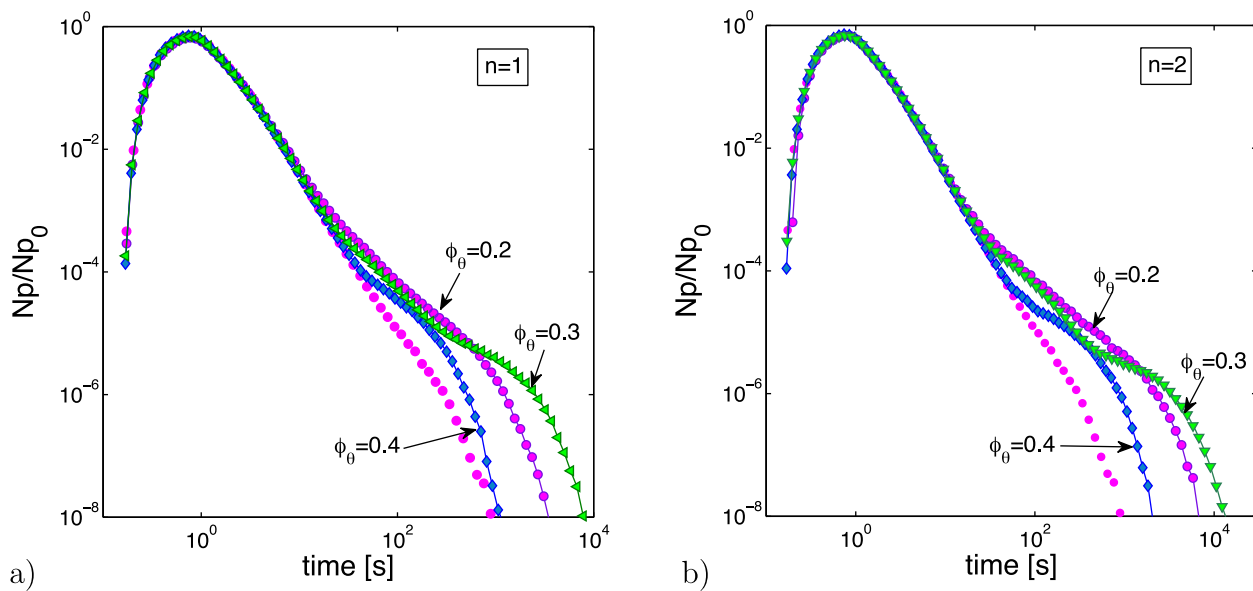


**Figure 12.** BTC computed in subvolume 3 (SV3) for  $Pe = 100$  and threshold values  $\phi_\theta = 0.2$  (connected pink circles),  $\phi_\theta = 0.3$  (green triangles), and  $\phi_\theta = 0.4$  (blue rhombus) with (a)  $n = 1$  and (b)  $n = 2$ . For comparison the unconnected pink circles denote the BTC in the absence of the microporous phase.

voxel of original image. The cross plot between coarse grained mean velocity from the fine mesh and its corresponding velocity in the resampled coarse mesh is presented in Figure 9a. These data are fitted by a linear trend of slope 0.89 indicating that, on average, velocities on the fine mesh are around 10% lower than those for the coarse mesh.

Figure 9b displays the comparison of the PDFs for the two different mesh resolutions. While no noticeable difference for low velocities is evidenced, the difference is more marked for higher velocity values. Whereas it can be conjectured that these differences in the higher velocity explain the difference in the BTC maximum concentration arrival time, the increase of the BTC tailing for the coarse mesh cannot be directly explained by the difference in the velocity PDF without a more detailed analysis of, for instance, the velocity correlation. This, however, is not the scope of this paper. Nevertheless, these results indicate clearly that refining the mesh

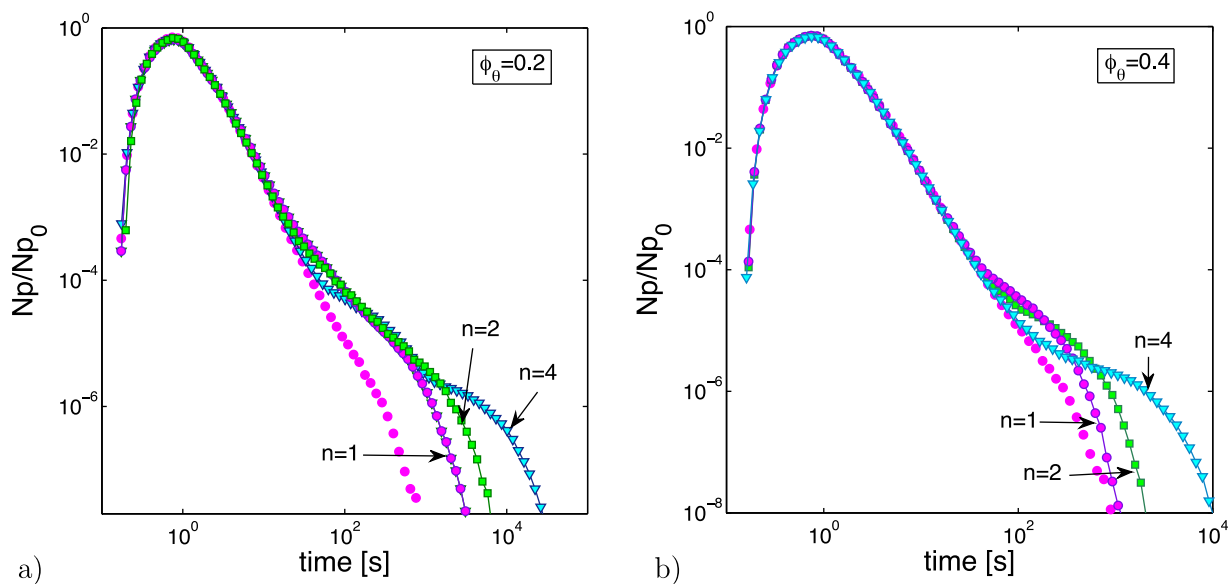


**Figure 13.** BTC for subvolume 3 (SV3) with  $Pe = 100$ . The parameters  $n$  and  $\phi_\theta$  defined in equation (14) for the effective diffusion coefficient are set to:  $n = 1$  (connected pink circles),  $n = 2$  (green squares) and  $n = 4$  (blue triangles); for (a)  $\phi_\theta = 0.2$ , and (b)  $\phi_\theta = 0.4$ . For comparison, the unconnected pink circles denote the BTC in the absence of the microporous phase.

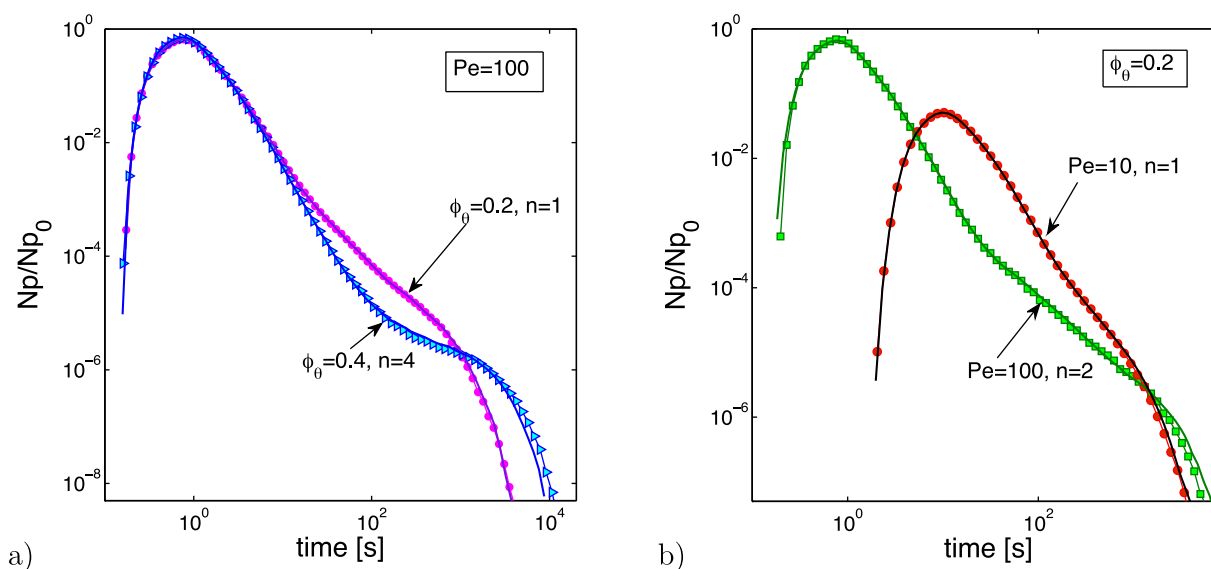


**Figure 14.** Comparison of the BTC in subvolume 3 (SV3) for a heterogeneous microporous phase characterized by spatially variable porosity  $\phi_\mu(\mathbf{x})$  (connected symbols) and in a homogeneous microporous phase characterized by the harmonic mean of  $\phi_\mu(\mathbf{x})$  (continuous thick line). (a) BTC with  $Pe = 100$  for  $\phi_\theta = 0.4$ ,  $n = 4$  (heterogeneous: blue triangles, homogeneous: blue thick line) and  $\phi_\theta = 0.2$  and  $n = 1$  (heterogeneous: pink circles, homogeneous: violet thick line). (b) BTCs with  $\phi_\theta = 0.2$  for  $Pe = 10$  and  $n = 1$  (heterogeneous: red circles, homogeneous: black thick line) and  $Pe = 100$ ,  $n = 2$  (heterogeneous: green squares, homogeneous: green thick line).

is not only important for improving the accuracy of flow field computation, but also for improving transport computation precision. Accordingly, all the following results were obtained using the fine mesh.

#### 4.2. Control of the Microporous Material on Transport

In this section, we investigate the control of the immobile domain on the overall transport of a passive tracer. Figure 10 displays the simulation results presented as the comparison of the BTC for the 4 subvolumes with and without the immobile domain for  $Pe = 100$ .

We observe very similar transport behaviors for all subvolumes in the case of mobile transport only. The BTCs are characterized by long-time tails with slope of  $t^{-2.4}$  for all four subvolumes indicated by the unconnected symbols in Figure 10. Conversely, when including the immobile domains (connected symbols) we observe that the difference from one subvolume to the other is much more marked than for transport in the mobile domain only.

The most significant difference between the mobile-only and mobile-immobile simulations appears in the tails. We observe a stronger tailing due to a larger proportion of slow transport, and the presence of two inflections points at the time  $t_1$  which marks the transient regime characterized by slopes smaller than  $t^{-2.4}$ ,

and the cut-off time  $t_2$  which denotes the diffusion time scale at which the mobile and immobile zones equilibrate. However both the slope and the value of  $t_2$  differ between subvolumes.

From the data reported in Table 2 we observe that the influence of the immobile domain on the intermediate slope of the BTC tail, which appears to be related mainly to the surface area  $\sigma_{m-im}$  of the interface between the mobile and immobile domains, albeit the influence of the immobile domain volume  $V_{im}$  is less clear-cut. Nevertheless, one can observe that SV4 is characterized by the largest values of both  $\sigma_{m-im}$  and  $V_{im}$  while the corresponding BTC (blue squares in Figure 10) displays a lower slope and value of  $t_2$ .

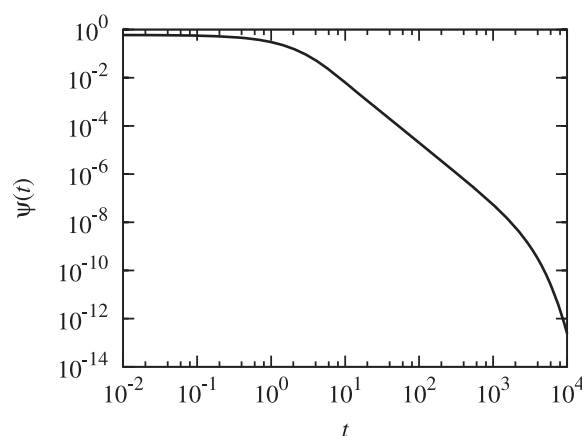


**Figure 15.** Illustration of the truncated power-law PDF (24) for  $\tau'_v = 1$  and  $\tau_c = 10^3$ .

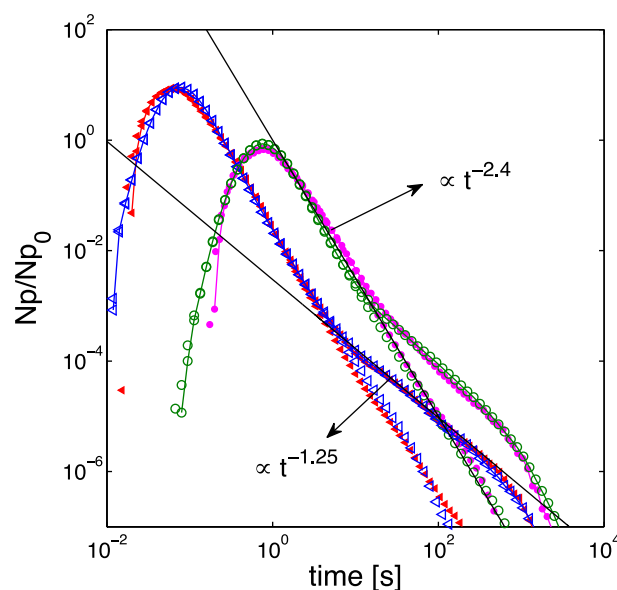


**Figure 16.** BTC for subvolume 3 (SV3) for  $Pe=10^3$  (filled red triangles), and  $Pe=10^2$  (filled pink circles) compared to the BTC obtained from the 1-D CTRW model (unfilled triangles and circles). Unconnected symbols denote the BTCs in the absence of the microporous phase. Connected symbols denote the BTCs in the presence microporous phase with  $n = 1$  and  $\phi_\theta = 0$ . The parameters for the 1-D CTRW model are  $b = 0.7$ , and  $\alpha = 0.3$ ,  $\alpha = 1.4$ ,  $\epsilon = 6 \times 10^{-5}$  for the PDF (24) of mobile times, a trapping frequency of  $\gamma = 0.05 \text{ s}^{-1}$ , and  $\beta = 0.25$ ,  $\tau_1 = 3 \text{ s}$  and  $\tau_2 = 700 \text{ s}$  for the PDF (26) of trapping times.

Figure 11 displays the comparison between the simulation (for SV3) of the mobile-only and the mobile-immobile cases for different values of the Peclet number ( $Pe = 0.1, 10, 100$ , and  $1000$ ). The elongation of the BTC tail and the occurrence of a second slope between  $t_1$  and  $t_2$  are clearly visible for  $Pe \geq 10$ . As expected, the difference between the two cases becomes insignificant for diffusion dominated transport ( $Pe \leq 0.1$ ); the only difference when adding the immobile domain is a small increase of about 5% (see Table 1) of the overall diffusional volume. The additional tailing behavior increases with the value of  $Pe$ .

These results clearly demonstrate the importance of the immobile domain, or in other words, the necessity of taking into account the presence of the microporous material, even if it represents a small fraction of the porosity. Also, the results indicate that the area of the interface between the mobile and the immobile domains is a critical parameter. The area of this interface determines the efficiency of mass transfer between these two domains, while the volume of the clusters which form the immobile domain should control the maximum (and average) trapping time in the immobile domain [Haggerty and Gorelick, 1995; Carrera et al., 1998]. However, this last statement cannot be verified by comparing the four subvolumes, because first the difference in terms of  $V_{im}$  is probably not significant and second we do not have precise information on the size of the immobile domain clusters.

#### 4.3. Effect of the Immobile Domain Properties on the BTC

As explained in section 3.3, the effective diffusion coefficient in the microporous material is evaluated from the distributed porosity (which is the only known property of this material) using the model described by

**Table 2.** Area  $\sigma$  of (Column 1) the Interface Between the Mobile Domain and the Microporous Material ( $\sigma_{m-im}$ ), (Column 2) the Mobile Domain and the Solid ( $\sigma_{m-s}$ ) and (Column 3) the Solid and the Immobile Domain ( $\sigma_{s-im}$ ) for Subvolumes SV1–SV4<sup>a</sup>

	Area in $\text{mm}^2$			Volume in $10^6 \mu\text{m}^3$	
	$\sigma_{m-im}$	$\sigma_{m-s}$	$\sigma_{s-im}$	$V_m$	$V_{im}$
SV1	0.77	1.62	1.10	164.9	24.9
SV2	0.76	1.61	1.04	164.6	23.1
SV3	0.71	1.71	1.04	155.5	21.8
SV4	0.84	1.58	1.19	155.2	26.4

<sup>a</sup>Columns 4 and 5 gives the volume of the mobile domain ( $V_m$ ) and of the immobile domain ( $V_{im}$ ) respectively.

(14). This model requires fixing both the porosity threshold  $\phi_\theta$  and the exponent  $n$  of the power law model (13). Here both these parameters are unknown. Yet their pertinent range can be deduced from the literature, which allows us to propose a meaningful sensitivity analysis of these parameters, here performed on subvolume SV3.

Figure 12 displays the BTCs for different percolation thresholds  $\phi_\theta=0.1, 0.3$  and  $0.4$  for  $n=2$  and  $4$ . Figure 13 displays the BTCs for different values of the exponent  $n$  ranging from  $1$  to  $4$  for  $\phi_\theta=0.2$  and  $0.4$ . Note that the BTCs for  $\phi_\theta=0.2$  and  $\phi_\theta=0$  are identical, compare Figure 11 and Figure 12. This is so because setting the value of  $\phi_\theta$  to  $0.2$  removes only a relatively small fraction of the microporous material, which is already difficult to be reached by the tracer due to its low diffusivity. Consequently, this does not modify noticeably the diffusion properties of the immobile domain. We observe a stronger tailing of the BTC as the value of  $\phi_\theta$  increases. Increasing the value of  $\phi_\theta$  means increasing the nondiffusive portion of the microporous region, and thus the its tortuosity. As a consequence, the tortuosity of the particle paths leads to an increase in the characteristic retention times and thus the observed stronger tailing of the BTC for  $\phi_\theta=0.3$  compared to  $\phi_\theta=0.2$ . Note that increasing the value of  $\phi_\theta$  also means decreasing the microporous domain volume. Thus, as the value of  $\phi_\theta$  is further increased, the immobile domain volume decreases to a point that its impact on transport becomes negligible. We observe this in Figure 12. For  $\phi_\theta \leq 0.4$  the BTC tailing is less pronounced than for  $\phi_\theta=0.3$ . Conversely, Figure 13 shows that increasing the value of  $n$  increasing the value of  $t_2$  (and to a lesser extent of  $t_1$ ), and decreases the slope of the intermediate regime bounded by  $t_1$  and  $t_2$ . This can be explained by the fact that increasing  $n$  corresponds to an increase of the width of the distribution of the effective diffusion coefficient in the immobile domain. Thus a larger fraction of low diffusion coefficient leads to a stronger particle retention and a larger cut-off time, which is set by the smallest diffusion coefficients.

#### 4.4. Equivalent Homogeneous Microporosity

Here we evaluate if the distributed porosity  $\phi_\mu(\mathbf{x})$  in the microporous phase can be simplified by an equivalent homogeneous porosity  $\phi_\mu^*$ . For this purpose, we compare simulations using a spatially variable porosity in the microporous phase with simulations that are characterized by the arithmetic, geometric and harmonic means of  $\phi_\mu(\mathbf{x})$ . Figure 14 shows that the spatially-distributed porosity in the microporous phase can be in general replaced by a constant porosity value equal to the harmonic mean. The effect of this simplification on the BTC shape is negligible for  $\phi_\theta=0.2$  and  $n=1$ , while in other cases (e.g., for  $\phi_\theta=0.4$ ,  $n=4$  and  $Pe=10$ ) second-order differences on the late-time BTC shape can be identified.

From Figure 14 we can conclude that in general the spatially variable  $\phi_\mu(\mathbf{x})$  can be substituted by an equivalent homogeneous value equal to harmonic mean of the spatial distribution of  $\phi_\mu(\mathbf{x})$ .

#### 4.5. Effective 1-D CTRW Model

We model the observed breakthrough curves by an effective  $d=1$  dimensional CTRW that accounts for both the impact of heterogeneous advection in the pore-space and particle retention due to mass transfer in the immobile domain. Particle transitions are modeled by the recursion relations

$$x_{n+1}=x_n+\Delta x_n, t_{n+1}=t_n+\Delta t_n \quad (16)$$

The increments  $\Delta x_n$  are identical independently distributed random variables which are characterized by the PDF

$$p_x(\Delta x)=(1-p_v)\delta(\Delta x-\ell)+p_v\delta(\Delta x+\ell), \quad (17)$$

where the probability  $p_v$  to move upstream is given by

$$p_v=\frac{1}{2+Pe_\ell}. \quad (18)$$

We defined here  $Pe_\ell=v\ell/d_0$ , where  $\ell$  is the transition length and  $v=b\bar{u}$  the effective flow velocity with  $b$  a modeling parameter of the order of  $1$  and  $\bar{u}$  the average pore velocity. Before specifying the transition length  $\ell$ , we recall that the particle velocities at subsequent steps in this modeling framework are assumed to be independent. We choose  $\ell=78.75 \mu\text{m}$ , which corresponds to half of the characteristic length  $L$  computed from the Berea sandstone pore structure (see section 3.5). Note that  $\ell$  is larger than the maximum pore radius ( $20 \mu\text{m}$ ), which we deem to be a suitable decorrelation length [de Anna et al., 2013; Kang et al., 2014].

To account for particle transitions in the mobile and immobile regions, the transition times  $\Delta t$  are modeled as [Margolin *et al.*, 2003; Benson and Meerschaert, 2009; Dentz *et al.*, 2012]

$$\Delta t = \tau_m + \sum_{i=1}^{n_{\tau_m}} \tau_{im,i}. \quad (19)$$

The mobile times  $\tau_m$  and immobile times  $\tau_{im,i}$  are each identical independently distributed random variables characterized by the PDFs  $\psi_m(\tau_m)$  and  $\psi_{im}(\tau_{im})$ , respectively. Note that  $n_{\tau_m}$  is the number of trapping events that occur in the time  $\tau_m$ . It is a Poisson random variable characterized by the probability distribution

$$p_n(n|\tau_m) = \frac{(\gamma\tau_m)^n \exp(-\gamma\tau_m)}{n!}, \quad (20)$$

where the trapping frequency  $\gamma$  is a modeling parameter that in principle may be related to the medium characteristics [Dentz *et al.*, 2012]. Note that the average number of trapping events is given by  $\gamma\tau_m$ , i.e., it depends on the mobile time, and thus on the flow conditions. The mobile time is modeled as

$$\tau_m = \tau_0 \eta, \quad (21)$$

in which  $\tau_0$  is an exponentially distributed random variable such that

$$\psi_0(\tau_0) = \frac{\exp(-\tau_0/\tau_v)}{\tau_v}, \quad \tau_v = \frac{\ell/v}{1+2Pe_\ell}. \quad (22)$$

The time  $\tau_v$  is the characteristic transition time for a Fickian model that is characterized by  $\eta = 1$ . In this case, the CTRW (16) describes advective-diffusive transport in a  $d = 1$  dimensional homogeneous medium characterized by the dispersion coefficient  $d_0$  and velocity  $\bar{u}$ . Note that the time  $\tau_v$  depends on both the average flow velocity as well as the diffusion coefficient. Thus, a change in the flow regime manifests directly in the distribution of transition times in the mobile domain.

The dimensionless time  $\eta$  accounts for a broad distribution of transport time scales and is here modeled by the truncated Pareto distribution

$$\psi_\eta(\eta) = \frac{\alpha}{a(1-\epsilon^\alpha)} \left(\frac{\eta}{a}\right)^{-1-\alpha}, \quad (23)$$

for  $a < \eta < a\epsilon^{-1}$ ; where  $a$  and  $\epsilon$  are a modeling parameter that in principle can be related to the smallest and the largest particle velocities. Thus, the PDF of mobile transition times  $\tau_m$  is given by

$$\psi_m(\tau_m) = \frac{\alpha}{\tau'_v(1-\epsilon^\alpha)} \left(\frac{\tau_m}{\tau'_v}\right)^{-1-\alpha} F_c(\tau_m, \tau'_v, \tau_c), \quad (24)$$

where we defined  $\tau'_v = a\tau_v$  and the cutoff time  $\tau_c = \tau'_v/\epsilon$ . The cut-off function  $F_c(\tau_m, \tau'_v, \tau_c)$  is defined by

$$F_c(\tau_m, \tau'_v, \tau_c) = \int_{\tau_m/\tau_c}^{\tau_m/\tau'_v} d\tau \tau^\alpha \exp(-\tau). \quad (25)$$

This distribution is constant for  $\tau_m < \tau'_v$ , then it decreases as the power-law  $\sim \tau_m^{-1-\alpha}$  until it is cut-off exponentially fast for times  $\tau_m > \tau_c$ , as illustrated in Figure 15. Thus, the fast time scales are delineated by the time scale  $\tau'_v$ , which scales with the mean flow velocity  $\bar{u}$  and the Peclet number. The upper cutoff scale is related to the smallest particle velocity

The immobile times  $\tau_{im}$  are modeled a the truncated power-law PDF of the same shape as (24),

$$\psi_{im}(\tau_{im}) = \frac{\beta}{\tau_1(1-\epsilon_{im}^\beta)} \left(\frac{\tau_{im}}{\tau_1}\right)^{-1-\beta} F_c(\tau_{im}, \tau_1, \tau_2), \quad (26)$$

where  $\tau_1 < \tau_{im} < \tau_2$ . The ratio between the lower and upper cut-off scales is denoted by  $\epsilon_{im} = \tau_1/\tau_2$ . The trapping rate and average trapping time may be related to the volume fraction  $\chi_{im}$  of the immobile domain as  $\chi_{im} = \gamma\langle\tau_{im}\rangle$ . The cutoff scales  $\tau_1$  and  $\tau_2$  as well as the exponent  $\beta$  are characteristic for the heterogeneity



of the immobile regions [Gouze *et al.*, 2008a]. Their values are estimated here from the simulated breakthrough curves.

This  $d = 1$  dimensional CTRW model provides a good description of the breakthrough curves obtained numerically from the flow and transport simulations in the heterogeneous pore structure as illustrated in Figure 16. Specifically, it reproduces very well the occurrence of two anomalous time regimes. The first reflects the velocity heterogeneity in the mobile medium portions in which the BTC scales as  $t^{-2.4}$ , while the second is characteristic of particle retention in the microporous immobile regions. In this regime, the BTC scales as  $t^{-5/4}$ .

The velocity heterogeneity in the CTRW model (16)–(26) is characterized by the exponent  $\alpha$ , which here is found to be  $\alpha = 1.4$ . The heterogeneity of the immobile zones is reflected by the exponent of  $\beta$ , which here is estimated as  $\beta = 1/4$  from the simulation data. This value indicates strong particle retention in the immobile regions. Note that mass transfer between a single type of homogeneous immobile region and the mobile domain is characterized by an exponent of  $\beta = 1/2$ , which leads to a BTC scaling as  $t^{-3/2}$ . The heterogeneity of the microporous immobile regions triggers stronger tailing than expected for homogeneous immobile regions.

The parameter values are estimated for the data set with  $Pe = 10^2$  and listed in the caption of Figure 16. The same parameters are used for the data set with  $Pe = 10^3$ , which provides an equally good fit. Thus, the modeling parameters of the effective CTRW model are characteristic of the medium heterogeneity because they do not change with the flow and transport conditions.

## 5. Conclusion

We presented a numerical study of pore-scale flow and transport of a passive tracer in porous sandstones based on high-resolution 3-D XRMT images of Berea sandstone samples. This rock contains a small fraction of a micro-porous phase which is defined as a porous material with pore smaller than the XRMT resolution. The simulations were performed on a set of subsamples, whose volumes are sufficiently large to be a pertinent approximation of the REV of the media. We obtained a suite of results that allowed us to determine and discuss, as far as we know for the first time, the respective role of the flow field heterogeneity in the macro-pore network, and mass transfer between the mobile and immobile domains.

The main results presented in this paper are:

1. As expected, the mesh resolution has an important influence on the transport results, independently of the presence of the micro-porosity; a coarse mesh tends to increase the non-Fickian behavior and specifically over-estimates the BTC tailing. However, we observed that the differences in non-Fickian behaviors for different mesh resolutions are more pronounced for low Peclet numbers. This is a priori counter-intuitive because a major implication of refining the mesh was a change (decrease) in permeability. Yet the differences in the PDFs of velocity between the coarse mesh and the fine mesh (corresponding to the subdivision of the cells of the coarse mesh in 27 subcells) appears to be small and consists mainly in a general shift of the velocity PDF, i.e., a change of the average velocity.
2. In the absence of mass transfer between the mobile and immobile domains, i.e., for transport localized in connected porosity only, we observed that the heterogeneity of the flow field triggers BTC late-time slopes scaling as  $t^{-2.4}$ .
3. Marked additional tailing of the BTCs is observed when one takes into account the immobile domain which is formed by the microporous material and some macropores connected by this microporous phase. Specifically, at high  $Pe$  a second time regime develops in which the BTC scales as  $t^{-5/4}$ . Furthermore, the results show that the increase in the late-time component of the BTC is (1) positively correlated to the volume of the micro-porous phase and to the surface area of the mobile-immobile interface, and (2) more pronounced at high Peclet numbers, but cannot be neglected even in the case of diffusion dominated transport.
4. As the only information on the microporous phase given by the XRMT images is its porosity, we employed the parametric model (14) to relate porosity to the effective dispersion coefficients in the immobile region. We probed the impact of the porosity threshold  $\phi_0$ , which denotes the minimum porosity required for percolation in the microporous phase, and the exponent  $n$  which is used to model

the tortuosity-porosity power-law dependence and determines the width of the distribution of effective diffusion coefficients. The results showed that: (1) The BTC tailing shows a nonmonotonic behavior with an increase of  $\phi_0$ . The tailing behavior first increases with the value of  $\phi_0$  because of an increase of the diffusion path tortuosity, which is triggered by an increase in the lacunarity of the microporous phase. As  $\phi_0$  increases further the volume of the microporous phase becomes more and more negligible compared to that of the mobile domain and its impact on the BTC diminishes dramatically. (2) Increasing  $n$  increases the BTC tailing and affects the cut-off time scale  $t_2$ . This is due to the fact that increasing the value of  $n$  decreases the average effective diffusion coefficient and increases the width of its distribution. The larger fraction of low effective diffusion coefficients leads to the increased tailing and the observed increase in  $t_2$ .

5. The spatially variable  $\phi_\mu(\mathbf{x})$  can be replaced with its constant harmonic mean,  $\phi_\mu(\mathbf{x})$ . This may be convenient for simplifying the sensitivity analysis of the transport results to the parameters of the immobile domain in case that the distribution of the porosity in the immobile domain is difficult to evaluate due to low quality XMRT data, for example.
6. We built a macroscopic 1-D CTRW model that captures the dual control of flow field heterogeneity and mass transfer between the mobile and immobile domains on non-Fickian transport. The transition time is modeled as the sum of the mobile transition time and the retention time in the immobile domain. The distribution of mobile transition times depends both on the average flow rate and the diffusion coefficient in the mobile region. The broad distribution of transport time scales in the mobile domain, which is a consequence of the velocity heterogeneity, is modeled by a truncated power-law whose characteristic time scales are related to the characteristic advection and diffusion times in the mobile zones.

The number of trapping events in the microporous phase per transition is modeled as a Poisson process whose mean is proportional to the mobile transition time, and thus dependent on the flow rate. The total retention time in the immobile domain then is given by the sum of random trapping times. The distribution of trapping time scales, which is related to the heterogeneous diffusion in the immobile zones, is modeled as a truncated power-law whose cutoff scales can be related to the characteristic diffusion times in the microporous domains.

The CTRW model represents well the observed breakthrough behavior and predicts the existence of two time regimes for large Péclet numbers, as observed in the numerical simulations. The modeling parameters of the presented CTRW approach adjusted from the BTCs for a given Péclet number provide equally good fits when changing the flow and transport regimes. Thus, we suggest that they are characteristic of the medium heterogeneity.

7. All together, the results presented in this paper demonstrate the critical role of both the velocity field heterogeneity and particle retention due to diffusion-dominated transport in the microporosity on observed non-Fickian transport behaviors, even in a rock for which the micro-porous cement represents only a small fraction of the connected porosity. We can anticipate that the non-Fickian behavior due to the presence of the immobile domain should be even more significant in sandstone reservoirs containing larger fractions of microporous cements and in carbonate reservoirs where the microporosity usually represents several percents of the domain accessible to the tracer transport [Garing *et al.*, 2014].

## Acknowledgments

The authors wish to thank Paul Tafforeau for his help in the X-ray microtomography data acquisition at the European Synchrotron Radiation facility (ESRF, France). All data used in this work are available upon from the corresponding author, while details and codes for OpenFOAM are available at <http://openfoam.org/>. MD acknowledges the support of the European Research Council (ERC) through the project MHetScale (617511).

## References

- Adams, E. E., and L. W. Gelhar (1992), Field study of dispersion in a heterogeneous aquifer, 2. Spatial moment analysis, *Water Resour. Res.*, 28, 3293–3308.
- Arns, C. H., et al. (2005), Pore scale characterization of carbonates using X-ray microtomography, *SPE J.*, 10, 475–484.
- Bear, J. (1972), *Dynamics of Fluids in Porous Media*, Am. Elsevier, N. Y.
- Becker, M. W., and A. M. Shapiro (2003), Interpreting tracer breakthrough tailing from different forced-gradient tracer experiment configurations in fractured bedrock, *Water Resour. Res.*, 39(1), 1024, doi:10.1029/2001WR001190.
- Benson, D. A., and M. M. Meerschaert (2009), A simple and efficient random walk solution of multi-rate mobile/immobile mass transport equations, *Adv. Water Resour.*, 32(4), 532–539, doi:10.1016/j.advwatres.2009.01.002.
- Berkowitz, B., A. Cortis, M. Dentz, and H. Scher (2006), Modeling non-Fickian transport in geological formations as a continuous time random walk, *Rev. Geophys.*, 44, RG2003, doi:10.1029/2005RG000178.
- Bijeljic, B., and M. J. Blunt (2006), Pore-scale modeling and continuous time random walk analysis of dispersion in porous media, *Water Resour. Res.*, 42, W01202, doi:10.1029/2005WR004578.
- Bijeljic, B., A. H. Muggeridge, and M. J. Blunt (2004), Pore-scale modeling of longitudinal dispersion, *Water Resour. Res.*, 40, W11501, doi:10.1029/2004WR003567.
- Bijeljic, B., P. Mostaghimi, and M. J. Blunt (2011), Signature of non-fickian solute transport in complex heterogeneous porous media, *Phys. Rev. Lett.*, 107, 204502, doi:10.1103/PhysRevLett.107.204502.

- Bijeljic, B., P. Mostaghimi, and M. Blunt (2013a), Insights into non-Fickian solute transport in carbonates, *Water Resour. Res.*, **49**, 2714–2728, doi:10.1002/wrcr.20238.
- Bijeljic, B., A. Raeini, P. Mostaghimi, and M. Blunt (2013b), Predictions of non-Fickian solute transport in different classes of porous media using direct simulation on pore-scale images, *Phys. Rev. E*, **87**, 013011–1–013011–9, doi:10.1103/PhysRevE.87.013011.
- Blunt, M., B. Bijeljic, H. Dong, O. Gharbi, S. Iglauer, P. Mostaghimi, A. Paluszny, and C. Pentland (2013), Pore-scale imaging and modelling, *Adv. Water Resour.*, **51**, 197–216, doi:10.1016/j.advwatres.2012.03.003.
- Carrera, J., X. Sánchez-Vila, I. Benet, A. Medina, G. Galarza, and J. Guimerà (1998), On matrix diffusion: Formulations, solution methods, and qualitative effects, *Hydrogeol. J.*, **6**, 178–190.
- Churcher, P., P. French, J. Shaw, and L. Schramm (1991), Rock properties of Berea sandstone, baker dolomite and Indiana limestone, paper SPE 21044 presented at the SPE International Symposium on Oilfield Chemistry, Soc. of Pet. Eng., Richardson, Tex.
- Datta, S. S., H. Chiang, T. S. Ramakrishnan, and D. A. Weitz (2013), Spatial fluctuations of fluid velocities in flow through a three-dimensional porous medium, *Phys. Rev. Lett.*, **111**, 064501, doi:10.1103/PhysRevLett.111.064501.
- de Anna, P., T. L. Borgne, M. Dentz, A. M. Tartakovsky, D. Bolster, and P. Davy (2013), Flow intermittency, dispersion, and correlated continuous time random walks in porous media, *Phys. Rev. Lett.*, **110**(18), 184502, doi:10.1103/PhysRevLett.110.184502.
- Delay, F., and J. Bodin (2001), Time domain random walk method to simulate transport by advection-diffusion and matrix diffusion in fracture networks, *Geophys. Res. Lett.*, **28**, 4051–4054.
- Delay, F., P. Ackerer, and C. Danquigny (2005), Simulating solute transport in porous or fractured formations using random walk particle tracking, *Vadose Zone J.*, **4**, 360–379.
- de Marsily, G. (1986), *Quantitative Hydrogeology: Groundwater Hydrology for Engineers*, Academic, San Diego, Calif.
- Dentz, M., and B. Berkowitz (2003), Transport behavior of a passive solute in continuous time random walks and multirate mass transfer, *Water Resour. Res.*, **39**(5), 1111, doi:10.1029/2001WR001163.
- Dentz, M., A. Cortis, H. Scher, and B. Berkowitz (2004), Time behavior of solute transport in heterogeneous media: Transition from anomalous to normal transport, *Adv. Water Resour.*, **27**(2), 155–173.
- Dentz, M., T. LeBorgne, A. Engler, and B. Bijeljic (2011), Mixing, spreading and reaction in heterogeneous media: A brief review, *J. Contam. Hydrol.*, **120–121**, 1–17, doi:10.1016/j.jconhyd.2010.05.002.
- Dentz, M., P. Gouze, A. Russian, J. Dweik, and F. Delay (2012), Diffusion and trapping in heterogeneous media: An inhomogeneous continuous time random walk approach, *Adv. Water Resour.*, **49**, 13–22, doi:10.1016/j.advwatres.2012.07.015.
- Ederly, Y., A. Guadagnini, H. Scher, and B. Berkowitz (2014), Origins of anomalous transport in heterogeneous media: Structural and dynamic controls, *Water Resour. Res.*, **50**, 1490–1505, doi:10.1002/2013WR015111.
- Garing, C., L. Luquot, P. A. Pezard, and P. Gouze (2014), Electrical and flow properties of highly heterogeneous carbonate rocks, *AAPG Bull.*, **98**(1), 49–66.
- Gouze, P., Y. Melean, T. Le Borgne, M. Dentz, and J. Carrera (2008a), Non-Fickian dispersion in porous media explained by heterogeneous microscale matrix diffusion, *Water Resour. Res.*, **44**, W11416, doi:10.1029/2007WR006690.
- Gouze, P., T. Le Borgne, R. Leprovost, G. Lods, T. Poidras, and P. Pezard (2008b), Non-fickian dispersion in porous media: 1. Multiscale measurements using single-well injection withdrawal tracer tests, *Water Resour. Res.*, **44**, W06426, doi:10.1029/2007WR006278.
- Gouze, P., R. Leprovost, T. Poidras, T. L. Borgne, G. Lods, and P. A. Pezard (2009), Cofis and telog: New downhole tools for characterizing dispersion processes in aquifers by single-well injection-withdrawal tracer tests, *C. R. Geosci.*, **341**(10–11), 965–975, doi:10.1016/j.crte.2009.07.012.
- Guibert, R., M. Nazarova, P. Horgue, G. Hamon, P. Creux, and G. Debenest (2015a), Computational permeability determination from pore-scale imaging: Sample size, mesh and method sensitivities, *Transp. Porous Media*, **107**, 641–656.
- Guibert, R., P. Horgue, G. Debenest, and M. Quintard (2015b), A comparison of various methods for the numerical evaluation of porous media permeability tensors from pore-scale geometry, *Math. Geosci.*, **1–19**, doi:10.1007/s11004-015-9587-9.
- Haggerty, R., and S. M. Gorelick (1995), Multiple-rate mass transfer for modeling diffusion and surface reactions in media with pore-scale heterogeneity, *Water Resour. Res.*, **31**, 2383–2400.
- Haggerty, R., S. A. McKenna, and L. C. Meigs (2000), On the late time behavior of tracer test breakthrough curves, *Water Resour. Res.*, **36**, 3467–3479.
- Haggerty, R., W. S. Flemin, L. C. Meigs, and S. A. McKenna (2001), Tracer tests in a fractured dolomite 2. Analysis of mass transfer in single-well injection-withdrawal tests, *Water Resour. Res.*, **37**, 1129–1142.
- Haggerty, R., C. F. Harvey, C. F. von Schwerin, and L. C. Meigs (2004), What controls the apparent timescale of solute mass transfer in aquifers and soils? A comparison of experimental results, *Water Resour. Res.*, **40**, W01510, doi:10.1029/2002WR001716.
- Hebert, V., C. Garing, L. Luquot, P. A. Pezard, and P. Gouze (2015), Multiscale X-ray tomography analysis of carbonate porosity, *Geol. Soc. Lon. Spec. Pub.*, **406**(1), 61–79, doi:10.1144/SP406.12.
- Holzner, M., M. Willmann, V. Morales, and M. Dentz (2015), Intermittent Lagrangian velocities and accelerations in three-dimensional porous medium flow, *Phys. Rev. E*, **92**, 013015.
- Hoshen, J., and R. Kopelman (1976), Percolation and cluster distribution. I. Cluster labeling technique and critical concentration algorithm, *Phys. Rev. B Solid State*, **14**(8), 3438–3445.
- Iassonov, P., T. Gebrenegus, and M. Tuller (2009), Segmentation of X-ray computed tomography images of porous materials: A crucial step for characterization and quantitative analysis of pore structures, *Water Resour. Res.*, **45**, W09415, doi:10.1029/2009WR008087.
- Kandhai, D., D. Hlushkou, A. G. Hoekstra, P. M. A. Slood, H. Van As, and U. Tallarek (2002), Influence of stagnant zones on transient and asymptotic dispersion in macroscopically homogeneous porous media, *Phys. Rev. Lett.*, **88**, 234501–1–234501–4, doi:10.1103/PhysRevLett.88.234501.
- Kang, P., P. de Anna, J. Nunes, B. Bijeljic, M. Blunt, and R. Juanes (2014), Pore-scale intermittent velocity structure underpinning anomalous transport through 3-D porous media, *Geophys. Res. Lett.*, **41**, 6184–6190, doi:10.1002/2014GL061475.
- Le Borgne, T., D. Bolster, M. Dentz, P. de Anna, and A. Tartakosky (2011), Effective pore-scale dispersion upscaling with a correlated continuous time random walk approach, *Water Resour. Res.*, **47**, W12538, doi:10.1029/2011WR010457.
- Levy, M., and B. Berkowitz (2003), Measurement and analysis of non-Fickian dispersion in heterogeneous porous media, *J. Contam. Hydrol.*, **64**(3–4), 203–226, doi:10.1016/S0169-7722(02)00204-8.
- Maier, R. S., M. R. Schure, J. P. Gage, and J. D. Seymour (2008), Sensitivity of pore-scale dispersion to the construction of random bead packs, *Water Resour. Res.*, **44**, W06503, doi:10.1029/2006WR005577.
- Mangane, P. O., P. Gouze, and L. Luquot (2013), Permeability impairment of a limestone reservoir triggered by heterogeneous dissolution and particles migration during CO<sub>2</sub>-rich injection, *Geophys. Res. Lett.*, **40**, 4614–4619, doi:10.1002/grl.50595.

- Margolin, G., M. Dentz, and B. Berkowitz (2003), Continuous time random walk and multirate mass transfer modeling of sorption, *Chem. Phys.*, **295**, 71–80.
- Meigs, L. C., and R. L. Beauheim (2001), Tracer tests in a fractured dolomite: 1. Experimental design and observed tracer recoveries, *Water Resour. Res.*, **37**, 1113–1128, doi:10.1029/2000WR900335.
- Moroni, M., N. Kleinfelter, and J. H. Cushman (2007), Analysis of dispersion in porous media via matched-index particle tracking velocimetry experiments, *Adv. Water Resour.*, **30**(1), 1–15, doi:10.1016/j.advwatres.2006.02.005.
- Mostaghimi, P., B. Bijeljic, and M. Blunt (2012), Simulation of flow and dispersion on pore-space images, *Math. Geosci.*, **17**, 1131–1141.
- Neuman, S. P., and D. M. Tartakovsky (2008), Perspective on theories of anomalous transport in heterogeneous media, *Adv. Water Resour.*, **32**, 670–680, doi:10.1016/j.advwatres.2008.08.005.
- Noettinger, B., and T. Estebenet (2000), Up-scaling of double porosity fractured media using continuous-time random walks methods, *Transp. Porous Media*, **39**, 315–337.
- Øren, P.-E., and S. Bakke (2003), Reconstruction of berea sandstone and pore-scale modelling of wettability effects, *J. Pet. Sci. Eng.*, **39**(3–4), 177–199, doi:10.1016/S0920-4105(03)00062-7.
- Ovaysi, S., and M. Piri (2011), Pore-scale modeling of dispersion in disordered porous media, *J. Contam. Hydrol.*, **124**, 68–81, doi:10.1016/j.jconhyd.2011.02.004.
- Paganin, D., T. E. Mayo, S. C. Gureyev, P. R. Miller, and S. W. Wilkins (2002), Simultaneous phase and amplitude extraction from a single defocused image of a homogeneous object, *J. Microsc.*, **206**, 33–40.
- Patankar, S. V. (1980), *Numerical Heat Transfer and Fluid Flow*, Hemisphere Publ. Corp.
- Pisani, L. (2011), Simple expression for the tortuosity of porous media, *Transp. Porous Media*, **88**, 193–203.
- Russian, A., P. Gouze, M. Dentz, and A. Gringarten (2015), Multi-continuum approach to modelling shale gas extraction, *Transp. Porous Media*, **109**, 109–130, doi:10.1007/s11242-015-0504-y.
- Sanchez, S., P. E. Ahlberg, K. M. Trinajstić, A. Mirone, and P. Tafforeau (2012), Three dimensional synchrotron virtual paleohistology: A new insight into the world of fossil bone microstructures, *Microsc. Microanal.*, **18**, 1095–1105.
- Scheibe, T. D., W. A. Perkins, M. C. Richmond, M. I. McKinley, P. D. J. Romero-Gomez, M. Oostrom, T. W. Wietsma, J. A. Serkowski, and J. M. Zachara (2015), Pore-scale and multiscale numerical simulation of flow and transport in a laboratory-scale column, *Water Resour. Res.*, **51**, 1023–1035, doi:10.1002/2014WR015959.
- Scheven, U. M., D. Verganelakis, R. Harris, M. L. Johns, and L. F. Gladden (2005), Quantitative nuclear magnetic resonance measurements of preasymptotic dispersion in flow through porous media, *Phys. Fluids*, **17**(11), 214504-1–214504-5, doi:10.1063/1.2131871.
- Schlüter, S., A. Sheppard, K. Brown, and D. Wildenschild (2014), Image processing of multiphase images obtained via X-ray microtomography: A review, *Water Resour. Res.*, **50**, 3615–3639, doi:10.1002/2014WR015256.
- Schumer, R. D., M. Benson, M. Meerschaert, and B. Baeumer (2003), Fractal mobile/immobile solute transport, *Water Resour. Res.*, **39**(10), 1296, doi:10.1029/2003WR002141.
- Sen, P., and P. J. Basser (2005), Modeling diffusion in white matter in the brain: A composite porous medium, *Magn. Reson. Imaging*, **23**, 215–220.
- Shapiro, A. M. (2001), Effective matrix diffusion in kilometer-scale transport in fractured crystalline rock, *Water Resour. Res.*, **37**, 507–522, doi:10.1029/2000WR900301.
- Spirkovska, L. (1993), A summary of image segmentation techniques, technical report, National Aeronautics and Space Administration (NASA) Technical Memorandum 104022, Ames Research Center, Moffett Field, Calif.
- Tanino, Y., and M. J. Blunt (2012), Capillary trapping in sandstones and carbonates: Dependence on pore structure, *Water Resour. Res.*, **48**, W08525, doi:10.1029/2011WR011712.
- Taylor, S. G. (1953), Dispersion of soluble matter in solvent flowing slowly through a tube, *Proc. R. Soc. London, Ser. A*, **219**, 186–203.
- Weller, H., G. Tabor, H. Jasak, and C. Fureby (1998), A tensorial approach to computational continuum mechanics using object-oriented techniques, *J. Comput. Phys.*, **12**, 620–631, doi:10.1063/1.168744.
- Yoon, H., Q. Kang, and A. J. Valocchi (2015), Lattice Boltzmann-based approaches for pore-scale reactive transport, *Rev. Mineral. Geochem.*, **80**, 393–431.
- Zhou, Q., H.-H. Liu, F. J. Molz, Y. Zhang, and G. S. Bodvarsson (2007), Field-scale effective matrix diffusion coefficient for fractured rock: Results from literature survey, *J. Contam. Hydrol.*, **93**(1–4), 161–187, doi:10.1016/j.jconhyd.2007.02.002.